

COVER PAGE

Document downloaded by @DAEL

Fri Nov 27 12:07:55 2026
For personal use

When automatic English translation is provided, only the original document is authentic.
The EAA cannot be held responsible of any translation error

Bibliographical reference

Investigating the Scattered Wave due to Dipoles of an Operating Propeller by a Weighting-Iteration Method, Jui-Hsiang Kao, Acta Acustica **vol. 103** (Number 5), 2017, pp. 746-757

DOI
https://doi.org/10.3813/AAA.919103

Acta Acustica united with Acustica
Vol. 103 (2017) 746 – 757

DOI 10.3813/AAA.919103

Investigating the Scattered Wave due to Dipoles of an Operating Propeller by a Weighting-Iteration Method

Jui-Hsiang Kao
Department of Systems Engineering and Naval Architecture National Taiwan Ocean University Keelung, Taiwan, R.O.C. jhkao@mail.ntou.edu.tw

Summary
The main objective of this paper is to investigate the scattered waves from a ship hull due to the dipoles (i.e. unsteady forces) of an operating propeller. As the marine propeller is free from cavitation, the noise generated by such a ship is mainly due to the dipoles. According to the literature, only the radiation due to the dipoles of the operating propellers has been discussed, with no particular investigation into scattering. The unsteady forces of a propeller include three components: the axial thrust, the tangential torque force, and the radial force; but the radial force is generally omitted, because it is much smaller than the first two. This paper considers both the reflected noise from the free surface and the scattered noise from the ship's hull and applies the Discrete Wave Equation to predict acoustic pressure at both the far and near fields. For computation of the scattering problem, the study employs a weighting-iteration method in the time domain, which can solve the scattering problem with complex geometry. Finally, this research computes the dipole noise of a container ship radiated by the propeller and scattered from the ship's hull with a soft free surface.

PACS no. 43.30.Nb

1. Introduction

A propeller operating in a non-uniform wake field is one of the prime sources of a ship's underwater noise. When the propellers are free from cavitation, such as on oceanography research ships, submarines at diving depth, and warships at cruising speeds, the noises generated by dipoles dominate. The scatterings from an immersed body thus obviously interfere with the directly-radiating propagations. The aim of this paper is to investigate the acoustic field for these ships. Verification of the scattering characteristics of the dipoles can be applied in many fields such as remote sensing, sonar detecting, and marine environmental protection.

The speeds of these ships are less than 30 Kn. The Mach numbers for these ships are very small and always less than 0.01. For any other type of ship, the vessel speed is always under 50 Kn, and the Mach number is lower than 0.017. The Doppler effect can be unconsidered due to the small Mach number for marine propellers. Thus, the ships can be thought of as scatterers at rest. Consequently, as the underwater acoustic is measured in any cavitation tunnel, such as the largest one, HSVA, in Germany, the ship model is also at rest. Besides, the acoustic pressure generated by marine propellers can be governed by a linear wave equation due to a low Mach number. Many studies in the literature have looked into the computation of radiations due to dipoles of the propeller, but it is hard to find any paper that has analyzed the scattering from an immersed structure due to dipoles of the propeller. Seybert *et al.* [1], Seybert and Soenarko [2] and Chen and Hong [3] solved the scattering problems in the frequency domain, in which only one frequency could be treated at a time. Kinns *et al.* [4, 5, 6] arranged stationary monopoles and dipoles near a rigid hull in a linear wave equation to compute the pressure fluctuation on hull surfaces. Kehr and Kao [7] only discussed the radiations due to dipoles and did not include scattering due to dipoles. Kao and Kehr [8] published a robust and computationally efficient method based on the scattering potential in a time domain, which can treat multi-frequency scattered waves from underwater obstacles, even for a geometry with multiple sharp edges. The study by Kehr and Kao [9] completely investigated noise due to sources (i.e. propeller unsteady sheet cavitation) with a free surface and hull scattering effects for a real container. In [10], a potential-flow Boundary Element Method with measured hull-pressure data as input was applied to solve the scattered noise from the ship's hull, and the model experiments were also carried out. It was concluded that the computed hull-pressure fluctuations due to non-cavitating propellers is reasonably accurate as compared with the experimental data. The coupled fluid-structure interaction for the scattering waves of the

Received 23 December 2016,
accepted 24 July 2017.

© S. Hirzel Verlag · EAA

submarine was considered by the fast multipole algorithm (FMA) and Finite Element Method in [11]. For simple structures, a coupled model using the FMA will provide a substantial increase in the possible model size or frequency limit compared to traditional methods. A submarine model was calculated by FMA, and the results exhibited good agreement with those by the PAFEC software. Bi *et al.* [12] solved the transient acoustic radiation from an arbitrarily shaped source in the time domain using a cubic spline interpolation. In the study by Paula *et al.* [13], although the ship's underwater noise is predicted, there is no special discussion about the scattering effect of dipoles. Jang *et al.* [14] and Ianniello [15] examined the radiations of the operating propeller. Li *et al.* [16] presented a time-domain boundary integral equation framework to analyze the acoustic scattering from spherical objects in a homogeneous medium. Kao [17] solved the scattering problems of obstacles with sharp edges and indented surfaces by a weighting-iteration method in the time domain - a method that is suitable for ships, because the geometry their stern is complex and includes indented surfaces.

To prevent detection by sonar, the propellers of submarines at diving depth and warships at cruising speeds must be free from cavitation during the design process. Moreover, the cavitation number of a submarine at diving depth is very high due to high static pressure, and hence cavitation is impossible to be found. Propeller cavitation is also not allowed for a research ship in order to restrict any selfŰinterference with the equipped sonar. Though the source effect (i.e. cavitation) is stronger than the dipole effect, it disappears for submarines, warships, and research ships. Therefore, it is important to predict radiation and scattering due to the dipoles of these vessels in which propeller cavitation cannot be found.

This present paper demonstrates the noise due to propeller dipoles behind a container ship with a soft free surface and scattering effects. The radiated noise is calculated first according to Kehr and Kao [7]. Then the method used by Kao [17] is applied to solve the scattering effect and also to investigate the propagating characteristics of the dipole noise with scattering effects.

2. Solution of acoustic pressure generated by a propeller's unsteady forces

As shown in Figure 1, both the incident pressure wave radiated by the propeller and the wave scattered from the ship's hull are included for calculating the underwater acoustic field. The imaged propeller and ship's hull for the simulation of the soft free surface also contribute acoustic pressure to the field points.

2.1. Linear Acoustic Theory

The flow field is assumed to be compressible and inviscid. If the propeller's unsteady force (i.e. dipole) is assumed to be the only noise source, then the governing equation of

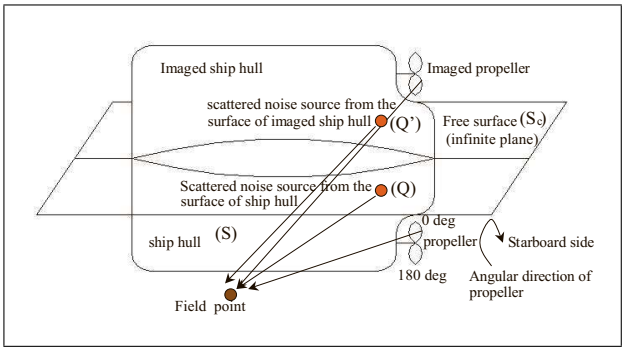


Figure 1. The schematic diagram of the solved problem.

the linear wave is

$$\nabla^2 p_{\text{load}} - \frac{1}{c_0^2}\frac{\partial^2 p_{\text{load}}}{\partial t^2} = \vec{\nabla}_s \cdot \vec{f}. \tag{1}$$

Here, p_{load} is the acoustic pressure due to the propeller's unsteady force, c_0 is the mean sound speed, $\vec{\nabla}_s$ is the vector gradient operator in noise source coordinates, and $\vec{f}$ denotes the unsteady force vector per unit volume acting on the fluid.

The solution to Equation (1) (Morse and Ingard 1968) can be expressed as integrals over the noise source volume V_S and noise source time t_S,

$$p_{\text{load}}(\vec{r}, t) = \tag{2}$$
$$-\frac{1}{4\pi}\int_{t_s=-\infty}^{\infty}\int_{\nabla_s}\frac{\vec{\nabla}_s \cdot \vec{f}(\vec{r}_s, t_s)}{R}\delta\Big(t_s - t + \frac{R}{c_0}\Big)\,\mathrm{d}V_s\,\mathrm{d}t_s,$$

where R is the distance from the noise source to the observer, δ is the Dirac delta function, and R/c_0 is the transmitting delay (or retarding) time between the noise source and the observer.

2.2. Noise Source

As shown in Figure 2, the rotating noise source with angular velocity Ω is located at position vector $\vec{r}_s(x_s, r_s, \theta_s = \theta_n - \Omega t_s)$ at t_s, and the observer is located at position vector $\vec{r}(x, r, \theta)$. Furthermore, the noise source is considered to be on the rotating propeller plane, i.e. $x_s = 0$. At time t_s, the dipole distribution strength corresponding to the unsteady forces, $\vec{f}$, on each blade n will be calculated by the propeller's unsteady lifting surface theory [18] PUF-3A, developed by MIT.

This paper does not consider the propeller's unsteady radial force, because it is relatively small compared with the unsteady thrust, f_x, and torque force f_θ. The total unsteady forces of a propeller at time t_s can then be represented by

$$f_x(t_s) = \sum_{m=1}^{B}\sum_{i=1}^{I}\sum_{j=1}^{J} T_{mij}(t_s), \tag{3}$$

$$f_\theta(t_s) = \sum_{m=1}^{B}\sum_{i=1}^{I}\sum_{j=1}^{J} \frac{Q_{mij}(t_s)}{r_s}, \tag{4}$$

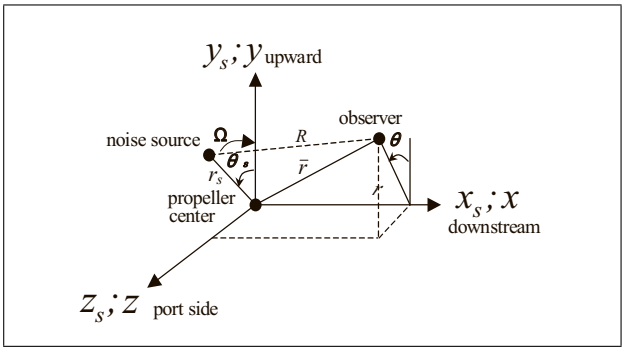


Figure 2. The cylinder's coordinate systems for the rotating noise source and the observer.

where B is the number of propeller blades, and the summation range for the mth blade is from hub to tip $(r_h \ldots r_t)$ and from leading edge to trailing edge $(\theta_l \ldots \theta_t)$. Moreover, $T_{mij}(t_s)$ and $Q_{mij}(t_s)$ are the respective axial thrust and tangential torque acting on the (i, j) element on the mth blade camber surface at time t_s.

2.3. Derivation of the Incident Pressure in the Free Field in the Time Domain

The distance from the noise source on the nth blade to the observer, R_n, in Figure 2 can be expressed as

$$R_n(t_s) = \sqrt{\left[(x-x_s)^2+r^2\right]+r_s^2-2r_s r\cos\left(\Omega t_s+\theta-\theta_n\right)}. \quad (5)$$

By letting $t_s = t - R/c_0$, the acoustic pressures due to the propeller's unsteady thrust and torque force at any field location and time t are respectively expressed as

$$p_T(\vec{r},t) = -\frac{1}{4\pi}\int_{V_s}\left[\frac{1}{R}\right]\left[\frac{\partial f_x}{\partial x_s}\right]\mathrm{d}V_s, \quad (6)$$

$$p_Q(\vec{r},t) = -\frac{1}{4\pi}\int_{V_s}\left[\frac{1}{R}\right]\left[\frac{1}{r_s}\right]\left[\frac{\partial f_\theta}{\partial \theta_s}\right]\mathrm{d}V_s. \quad (7)$$

The terms in Equations (6) and (7) (i.e. $[1/R]$, $[\partial f_x/\partial x_s]$ and $[\partial f_\theta/\partial\theta_s]$) are at the retarded time, t_s. These forces, f_x and f_θ, are dependent on the position of the discrete point dipole, $\vec{r}_s$, and the retarded time, t_s. By using Gauss's theorem [19, 20], the total acoustic pressure, induced by the unsteady thrust of all propeller blades, is obtained as

$$\begin{aligned} p_T(\vec{r},t) = &\sum_{m=1}^{B}\sum_{i=1}^{I}\sum_{j=1}^{J}\sum_{q=1}^{\infty}\cdots \\ &\left(\frac{(x_s-x)q\Omega}{4\pi\left[R^2\right]c_0}H_{mij}^{*q}\sin\left(q\left[\Omega(t_s)-\theta_n\right]+\varepsilon_{mij}^{*q}\right)\right. \\ &-\frac{(x_s-x)}{4\pi\left[R^3\right]}\left\{H_{mij}^{*0}+H_{mij}^{*q}\cos\left(q\left[\Omega(t_s)-\theta_n\right]+\varepsilon_{mij}^{*q}\right)\right\} \\ &+\frac{\Omega r_n r(x_s-x)}{4\pi c_0\left[R^4\right]}\sin\left(\Omega t_s+\theta-\theta_n\right) \\ &\left.\cdot\left\{H_{mij}^{*0}+H_{mij}^{*q}\cos\left(q[\Omega(t_s)-\theta_n]+\varepsilon_{mij}^{*q}\right)\right\}\right). \end{aligned} \quad (8)$$

Here, H^* and ε^* are the respective amplitude and phase angle of the thrust Fourier series.

We note that the acoustic pressure consists of three parts. The first part is proportional to the ratio of $(x - x_s)/[R^2]$ and depends on factor $q\Omega/c_0$. The second part is a higher-order term, which is proportional to the ratio of $(x - x_s)/[R^3]$ The third part is relationally small for marine propellers, both in near-field and far-field conditions, because it is proportional to $\Omega r_n/c_0$ and decays at the ratio of $r(x - x_s)/[R^4]$. When the distance, R, is far enough - that is, $1/[R]$ is much smaller than $q\Omega/c_0$ - the higher-order term decays very fast and the acoustic pressure will be proportional to $1/[R]$ in the same direction from the propeller center to the field point. At the near field, the second part plays an important role, and the frequency shift it causes will be apparent for the condition of each propeller blade. For a detailed deriving of Equation (8), please refer to [7].

The acoustic pressure, induced by the unsteady propeller torque force, can be similarly derived as

$$\begin{aligned} p_Q(\vec{r},t) = &\sum_{m=1}^{B}\sum_{i=1}^{I}\sum_{j=1}^{J}\sum_{q=1}^{\infty}\cdots \\ &\left(\frac{-q\Omega r}{4\pi\left[R^2\right]r_n c_0}H_{mij}^{'q}\sin\left(\Omega(t_s)+\theta-\theta_n\right)\right. \\ &\cdot\sin\left(q\left[\Omega(t_s)-\theta_n\right]+\varepsilon_{mij}^{'q}\right) \\ &+\frac{r}{4\pi r_n\left[R^3\right]}\left\{H_{mij}^{'0}+H_{mij}^{'q}\cos\left(q\left[\Omega(t_s)-\theta_n\right]+\varepsilon_{mij}^{'q}\right)\right\} \\ &\cdot\sin\left(\Omega(t_s)+\theta-\theta_n\right) \\ &-\frac{\Omega r^2}{4\pi c_0\left[R_n^4\right]}\left\{H_{mij}^{'0}+H_{mij}^{'q}\cos\left(q[\Omega(t_s)-\theta_n]+\varepsilon_{mij}^{'q}\right)\right\} \\ &\left.\cdot\sin\left(\Omega(t_s)+\theta-\theta_n\right)\right). \end{aligned} \quad (9)$$

This reveals that the acoustic pressure also includes three parts. Similarly, the first term, which is proportional to the ratio of $r/[R^2]$ and depends on the factor $q\Omega/c_0$ is due to the temporal variation of the torque force. The second term is proportional to the ratio of $r/[R^3]$ and decays faster than the first term at the far field. The third term is also negligibly small for marine propellers both in the near field and far field.

Because the third term in Equation (8) is negligible, the acoustic pressure due to the propeller's unsteady thrust depends on the axial direction, x, of the field points. The acoustic pressure, induced by the propeller's unsteady torque force, depends on two additional directions, r and θ, of the field points.

3. A weighting-iteration method for the acoustic scattering problem

This study applies a weighting-iteration method derived in the time domain for the time-harmonic scattering problem with multi-frequency incidents. In [17], the method is

suitable for complex-shaped scatterers with some reduced solid angles, with deviations of up to 30% from the standard value of 0.5.

The iteration scheme for the scattered wave pressure (P_S) in the time domain is proposed below.

$$\begin{aligned} C(P)\,P_S(P,t) &= \int_{-\infty}^{\infty}\int_S P_S(Q)\frac{\partial G(P,Q)}{\partial n}\,\mathrm{e}^{\mathrm{i}\omega t}\,\mathrm{d}S\,\mathrm{d}\omega \\ &\quad - \int_{-\infty}^{\infty}\int_S G(P,Q)\frac{\partial P_S(Q)}{\partial n}\,\mathrm{e}^{\mathrm{i}\omega t}\,\mathrm{d}S\,\mathrm{d}\omega \\ &= A_{\mathrm{part}}\big(P_S(P,t)\big) + B_{\mathrm{part}}\big(P_I(P,t)\big). \end{aligned} \tag{10}$$

Here, P_I is the incident wave pressure, and $G(P,Q)$ is the half-space Green function that depends on the locations of a field point, P, and a source point, Q,

$$G(P,Q) = \frac{1}{4\pi}\left(\frac{\mathrm{e}^{-\mathrm{i}kr}}{r} + R_H\frac{\mathrm{e}^{-\mathrm{i}kr_i}}{r_i}\right), \tag{11}$$

where r is the distance between P and Q, and r_i is the distance between P and Q', the imaged point of Q, as shown in Figure 1. The reflection coefficient, R_H, is equal to 1 for a rigid infinite plane and -1 for a soft infinite plane. Here, $C(P)$ in Equation (10) is the solid angle for the field point, P, and can be evaluated as

$$C(P) = 1 + \frac{1}{4\pi}\int_{S+S_c}\frac{\partial}{\partial n}\left[\frac{1}{r(P,Q)}\right]\mathrm{d}S, \tag{12}$$

if P is on a ship hull (S), but not in contact with a free surface (S_c), and

$$C(P) = \big(1+R_H\big)\left\{\frac{1}{2} + \frac{1}{4\pi}\int_{S+S_c}\frac{\partial}{\partial n}\left[\frac{1}{r(P,Q)}\right]\mathrm{d}S\right\}, \tag{13}$$

if P is at the intersection of S and S_c.

In Equation (10), A_{part} can be expressed in the time domain as

$$\begin{aligned} A_{\mathrm{part}} = \sum_{m=1}^{M}\Bigg\{ &\left[P_S(Q,t-r/c)\Big(\frac{-1}{r^2}\Big) - \frac{\partial P_S(Q,t-r/c)}{\partial t}\frac{1}{cr}\right]\cdot\big(\nabla\vec{r}\cdot\vec{n}\big) \\ &+ R_H\left[P_S(Q,t-r_i/c)\Big(\frac{-1}{r_i^2}\Big) - \frac{\partial P_S(Q,t-r_i/c)}{\partial t}\frac{1}{cr_i}\right]\cdot\big(\nabla\vec{r}_i\cdot\vec{n}_i\big)\Bigg\}_m\cdot\frac{\Delta S_m}{4\pi}. \end{aligned} \tag{14}$$

Because the solid boundary condition is applied and the incident potential is given, B_{part} in Equation (10) is presented as

$$\begin{aligned} B_{\mathrm{part}} &= \int_{-\infty}^{\infty}\int_S G(P,Q)\frac{\partial P_S(Q)}{\partial n}\mathrm{e}^{\mathrm{i}\omega t}\,\mathrm{d}S\,\mathrm{d}\omega \\ &= \int_{-\infty}^{\infty}\int_S G(P,Q)\frac{\partial P_I(Q)}{\partial n}\mathrm{e}^{\mathrm{i}\omega t}\,\mathrm{d}S\,\mathrm{d}\omega \\ &= \frac{1}{4\pi}\int_S\frac{1}{r}\frac{\partial P_I(Q,t-r/c)}{\partial n}\,\mathrm{d}S + \frac{R_H}{4\pi}\int_S\frac{1}{r_i}\frac{\partial P_I(Q,t-r_i/c)}{\partial n_i}\,\mathrm{d}S \\ &= \sum_{m=1}^{M}\Bigg\{\big[\nabla P_I(Q,t-r/c)\cdot\vec{n}\big]\frac{1}{r} + R_H\big[\nabla P_I(Q,t-r_i/c)\cdot\vec{n}_i\big]\frac{1}{r_i}\Bigg\}_m\cdot\frac{\Delta S_m}{4\pi}. \end{aligned} \tag{15}$$

In Equation (15), m presents different elements of the ship's hull, and the summation is carried out from $m = 1\ldots m = M$. The iteration scheme is based on Equation (10), and B_{part} in Equation (15) is known and calculated by the incident wave. An initial scattered potential, P_S, on the body equal to zero is first prescribed. Next, the scattered potential field on the body on the left-hand side of Equation (10) can be updated explicitly by calculating Apart according to Equation (14).

If the scatterer has a complex shape, then the solid angles of some panels on the complex structure will be reduced and clearly deviate from the standard value of 0.5. This makes it difficult for the iteration scheme of Kao and Kehr [8] to find a convergent result, and the convergence will be very slow. Therefore, this paper modifies the iteration scheme in Equation (10) by introducing a weighting-iteration method in the time domain to solve the scattering problems of complex objects.

By reformulating Equation (10), the iteration scheme can be re-presented as

$$\begin{aligned} P_S(P,t)_{n+1} &= \big[A_{\mathrm{part}}\big(P_S(P,t)\big) + B_{\mathrm{part}}\big(P_I(P,t)\big)\big]/C(P) \\ &= P_S(P,t)_n + \Delta P_S(P,t). \end{aligned} \tag{16}$$

The suffix $(.)_{n+1}$ indicates the values by the $(n+1)$th iteration, and $(.)_n$ presents the values by the nth iteration. The difference between the $(n+1)$th and nth iterations can be expressed as

$$\begin{aligned} \Delta P_S(P,t) &= \big[A_{\mathrm{part}}\big(P_S(P,t)\big) + B_{\mathrm{part}}\big(P_I(P,t)\big)\big]/C(P) \\ &\quad - P_S(P,t)_n. \end{aligned} \tag{17}$$

To speed up the convergence, a weighting function is introduced to Equation (16) as

$$P_S(P,t)_{n+1} = P_S(P,t)_n + W\,\Delta P_S(P,t). \tag{18}$$

The weighting function, W, is defined as

$$W = \big(0.5/\text{Solid angle}\big)^m. \tag{19}$$

This weighting function is only applied to panels with solid angles with values of less than 0.5. During the iteration process, the weighting function is used at first to

speed up the convergence and leads the convergence history toward the correct tendency. Once rough convergence is reached, subsequent iterations are conducted by the formal scheme, Equation (10), to obtain the correct result. Please refer to Kao [17] for details.

As the resonance frequencies are considered, the CHIEF method is a popular technique in the frequency-domain BEM. However, the CHIEF method is not suitable for the present scheme because the present scheme is time-domain BEM solving the radiated noise by iterations.

For conquering the non-uniqueness problem at resonance frequencies, the two methods below could be combined with the present iterating scheme.

(a) According to Stütz *et al.* [21], a new form of the Boundary Integral Equation is suggested for the time-domain BEM. Thus, Equations (14) and (15) can be reformulated as

$$A_{\text{part}} = \sum_{m=1}^{K}\sum_{n=1}^{N}\left\{\left[\frac{-1}{r^2}\left[(K-m+1)P_s^{n,m} - (K-m)P_s^{n,m-1}\right]\psi(t_{rK})\right]\cdot\left(\nabla\vec{r}\cdot\vec{n}\right) + R_H\left[\frac{-1}{r_i^2}\left[(K-m+1)P_s^{n,m} - (K-m)P_s^{n,m-1}\right]\psi(t_{r_iK})\right]\cdot\left(\nabla\vec{r}_i\cdot\vec{n}_i\right)\right\}_m\cdot\frac{\Delta S_n}{4\pi}. \tag{20}$$

$$B_{\text{part}} = \sum_{m=1}^{K}\sum_{n=1}^{N}\left[\frac{1}{r}\left(\nabla P_I^{n,m}\cdot\vec{n}\right)\psi(t_{rK}) + \frac{1}{r_i}\left(\nabla P_I^{n,m}\cdot\vec{n}\right)\psi(t_{r_iK})\right]\cdot\frac{\Delta S_n}{4\pi}, \tag{21}$$

$$\psi(t_{ri}) = \begin{cases} 1, & t_{rk} \text{ or } t_{r_iK} \in (t_{m-1}, t_m), \\ 0, & \text{else.} \end{cases} \tag{22}$$

The boundary surface is divided into N planar elements. In discretizing time itself in equidistant time steps $t_K = K\,\Delta t$ ($K = 1, 2, \ldots$), and the retarded time is obtained, $t_{rK} = K\,\Delta t - r/c$. A controlling factor β is defined.

$$\beta = c\,\Delta t/h. \tag{23}$$

Here h is the element size.

The present Weighting-Iteration Method can be carried out according to Equations (20) and (21) instead of Equations (14) and (15). The controlling factor β is not included in the Equations (20), (21), and (22); however, β is dependent on the distributions of elements and time steps. β is the ratio of the traveling distance of the wave at each time step to the maximum side length of the elements. In order to minimize error due to the resonance frequencies, Stütz *et al.* [21] suggest that β should be less than 0.5.

(b) Equation (10) can be replaced by the Burton-Miller type integral equation derived in [22]. The present Weighting-Iteration scheme can then be conducted according to the Burton-Miller type integral equation to prevent the numerical instability caused by the resonance frequencies. Please refer to Chappell *et al.* [22] for the detailed description of the Burton-Miller type integral equation.

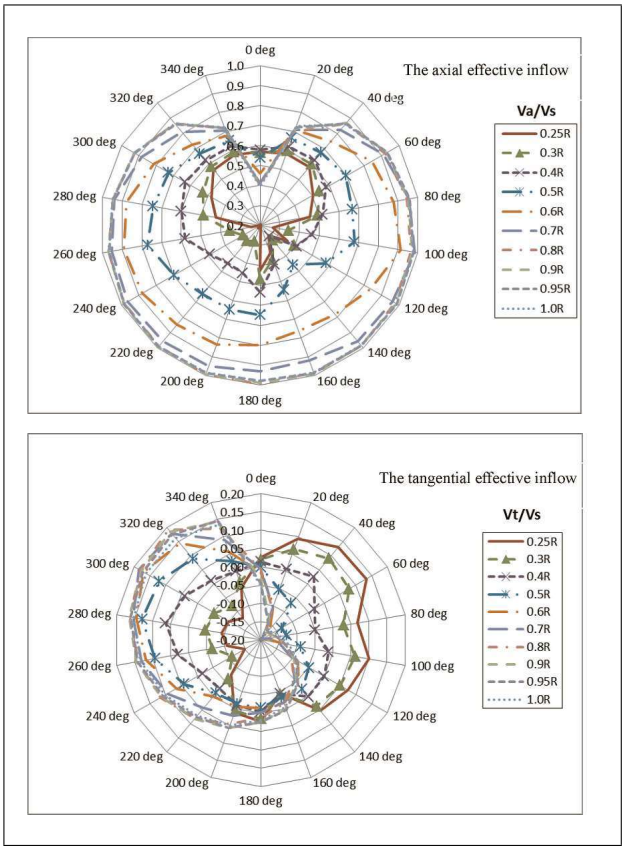


Figure 3. The effective inflow of the propeller for different radii at every angular position.

4. Dipole strength of the investigated propeller

The pressure fields induced by the propeller's unsteady thrust and torque force are now calculated. The effective axial and tangential inflow distributions of the propeller at different blade angles and radial positions are shown in Figure 3. The blade angle is viewed from the stern. The starboard side corresponds to 90 degrees, and the port side to 270 degrees. R is the propeller radius. The blade root is at $0.2R$, and blade tip is at $1.0R$. Both the axial and tangential inflows are nondimensionalized by the ship velocity, V_s. Each concentric circle represents a different velocity, emanating from a lower value at the center to higher ones at the outer circles. In Figure 3, the axial inflow near 0 degree is hindered most obviously by the stern; thus, the inflow value is the lowest. Because the tangential inflow of the ship is asymmetric, the values at 90 degrees and 270 degrees are opposite in sign.

The dipoles include the propeller's unsteady thrust and torque forces, and the radial force is relatively small and can be ignored. Figure 4 plots the unsteady thrust of a

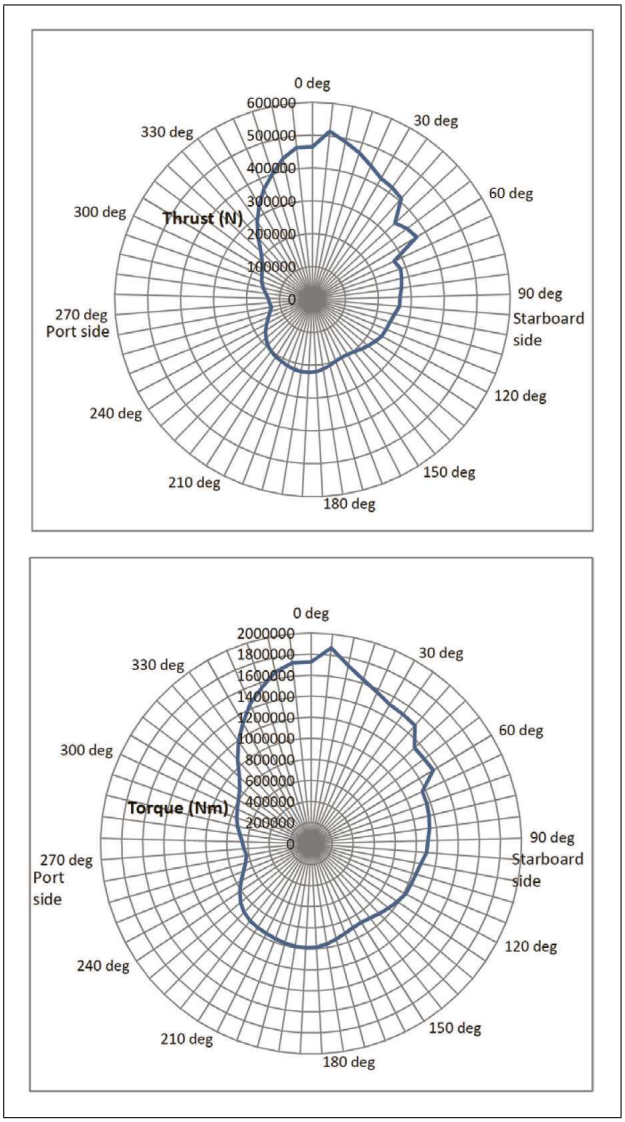


Figure 4. The unsteady loadings of the propeller for one blade at different angular positions.

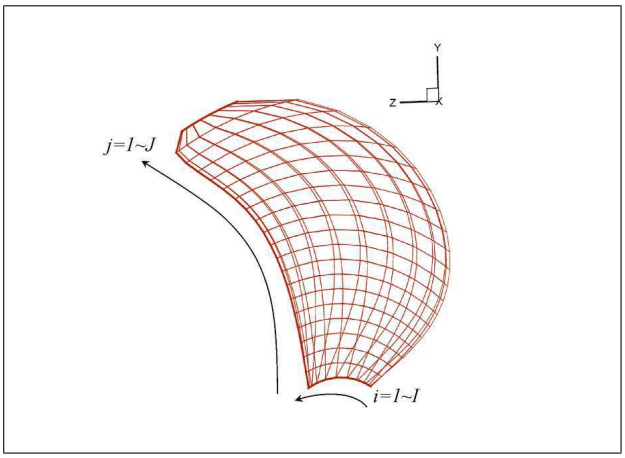


Figure 5. The elements on the propeller surface.

single blade at different angular positions, calculated by PUF-3A developed by Kerwin *et al.* [18]. The propeller

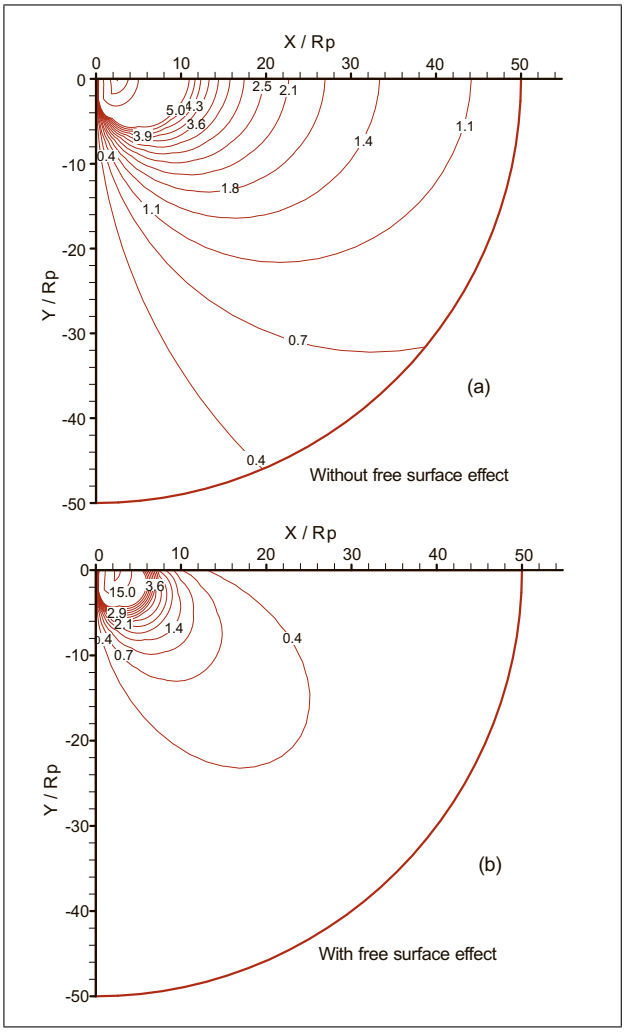


Figure 6. A contour plot of the amplitude for the first blade-rate harmonic due to the propeller's unsteady thrust in the X-Y plane (unit: Pa).

blade delivers a relatively large total thrust, near 15 degrees on the starboard side. This is due to the asymmetry in the tangential wake component for a single screw container ship. Figure 4 also presents the total unsteady torque of one blade, calculated by PUF-3A, at different angular positions. It can be seen that the distribution of torque is similar to that of the thrust.

Indeed, the force contributed by every element (i, j) on the propeller surface, as shown in Figure 5 at different blade angles, is considered during the computing process. The summations in Equations (8) and (9) both include i and j terms. However, the force contours plotted in Figure 4 only illustrate the total force summated by all elements $(I \times J)$ at different blade angles.

The associated data of this propeller are as follows:

Blade Number (NB):	6
Section Type:	NACA 66
RPM:	103.8
Pitch Ratio at $0.7R$:	1.07
Diameter (m):	7.18
AREA Ratio:	0.895

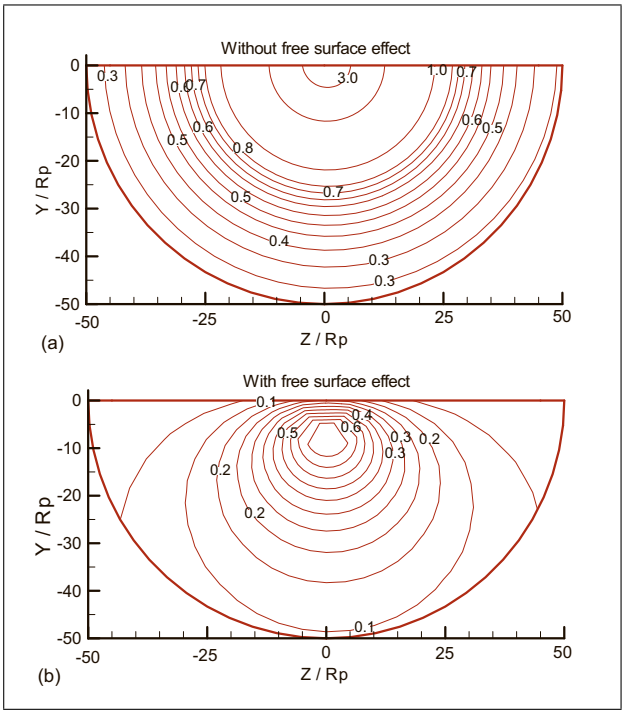


Figure 7. A contour plot of amplitude for the first blade-rate harmonic due to the propeller's unsteady thrust in the Y-Z plane at 15 Rp downstream from the propeller's center (unit: Pa).

5. Results of noise radiated by the propeller

Figures 6 (in X-Y plane) and 7 (in Y-Z plane) present the amplitude contour plots for the case of first blade-rate harmonics due to the propeller's unsteady thrust. The Y-Z plane is at X=15 Rp (Rp the propeller radius). The noise caused by the propeller dipoles is related to the blade-rate, and the first blade-rate usually dominates. The present propeller is 6-blade, and the rotating speed is 1.73RPS. Thus, the first blade-rate frequency is 10.38 Hz. Here, X's direction is downstream of the propeller shaft, Y's direction is upward, and Z's direction is portside. As shown by Figures 6a and 6b, the amplitude along the Y-axis is zero as both x and x_l are zero on the Y-axis. Furthermore, as the field points are located at the propeller axis and far downstream, the destructive interference due to the free surface is stronger. Thus, the dominant acoustic field generated by the propeller's unsteady thrust, considering the free surface effect, is essentially along the 45 degree direction to the X-axis in the X-Y plane and not along the X-axis.

The acoustic pressure contributed by the first and second terms of the right-hand side in Equation (8) is independent of the angular positions of the field points, θ. Because the first and second terms of the right-hand side of Equation (8) primarily contribute to the acoustic pressure, due to the propeller's unsteady thrust, the contour lines in Figure 7a (in the Y-Z plane) form concentric circles. The small asymmetry seen in Figure 7a is caused by the asymmetry in the tangential component of the wake flow shown in Figure 3. The contour lines in Figure 7b are symmetrical

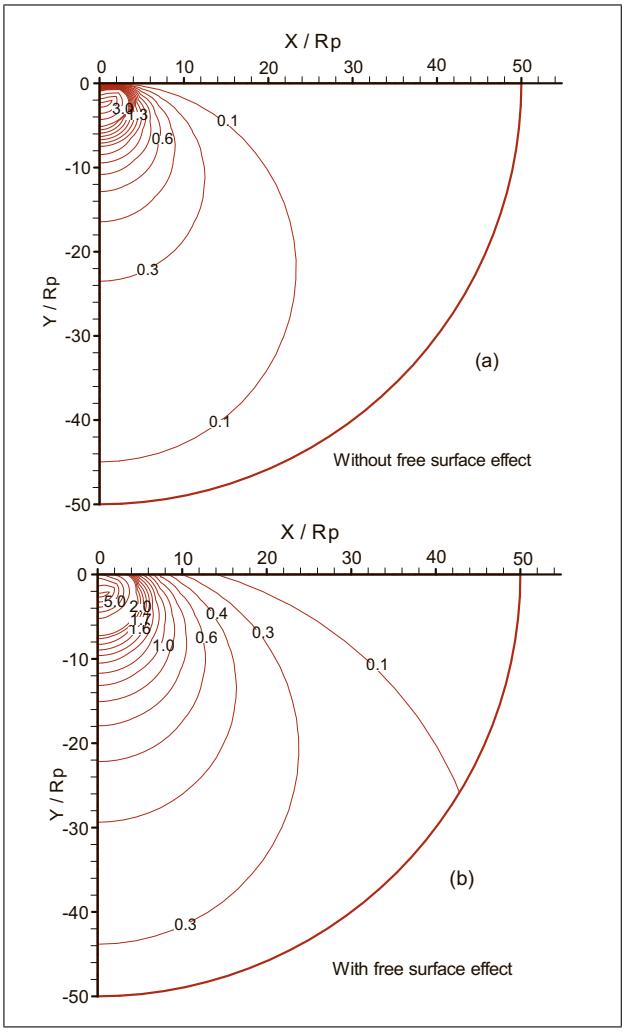


Figure 8. A contour plot of amplitude for the first blade-rate harmonic due to the propeller's unsteady torque force in the X-Y plane (unit: Pa).

with respect to the Y-axial in the Y-Z plane, and a strong destructive interference appears near the free surface.

Figures 8 and 9 present the amplitude contour plots caused by the propeller's unsteady torque force. Figure 8 shows the amplitude for the first blade-rate harmonic in the X-Y plane. The acoustic pressure induced by the propeller's unsteady torque force is dependent on r; thus, it vanishes along the propeller axis. However, it still has a small amplitude arising from the imaged propeller (r) as shown in Figure 8b, and it dominates along the Y-axis. Figure 9 shows the amplitude for the first blade-rate harmonic in the Y-Z plane. The acoustic pressure, due to the propeller's unsteady torque force, depends not only on the radial position of the field points, r, but also on the angular position, θ. Therefore, the contour lines in the Y-Z plane are not concentric circles.

In Figure 9a, although the radial distances, r, of the field points in the A zone are smaller than those in the B zone, the amplitudes in the A zone are larger than those in the B zone. This could be due to the distance factor – the noise sources are farther away for the B zone compared to the A zone. In Figure 9a, both the A and B zones appear on the

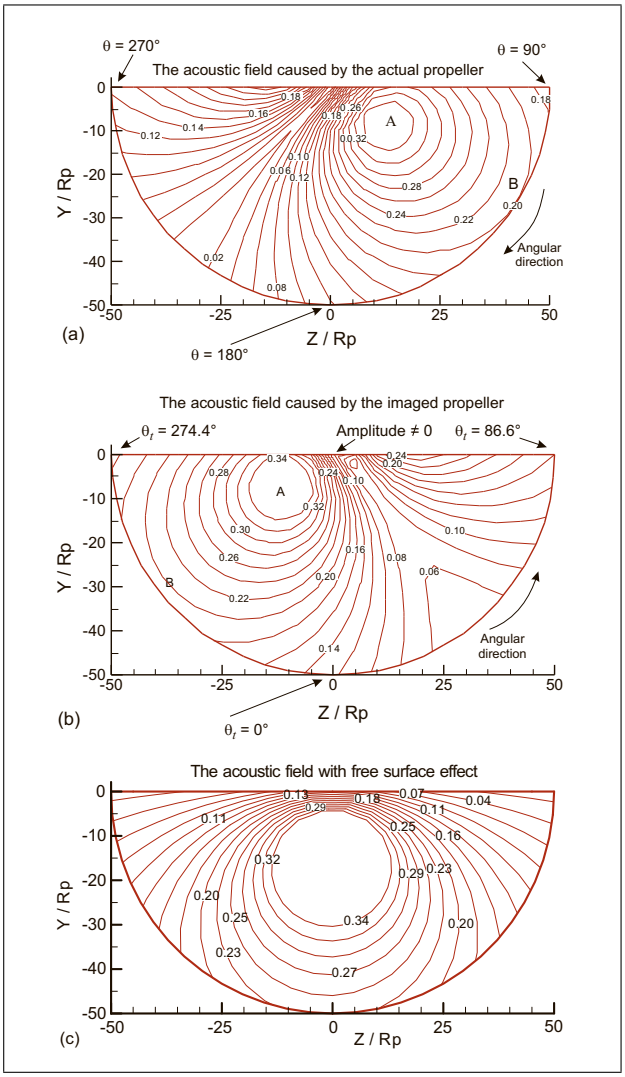


Figure 9. A contour plot of amplitude for the first blade-rate harmonic due to the propeller's unsteady torque force in the Y-Z plane at 15 Rp downstream from the propeller's center (unit: Pa).

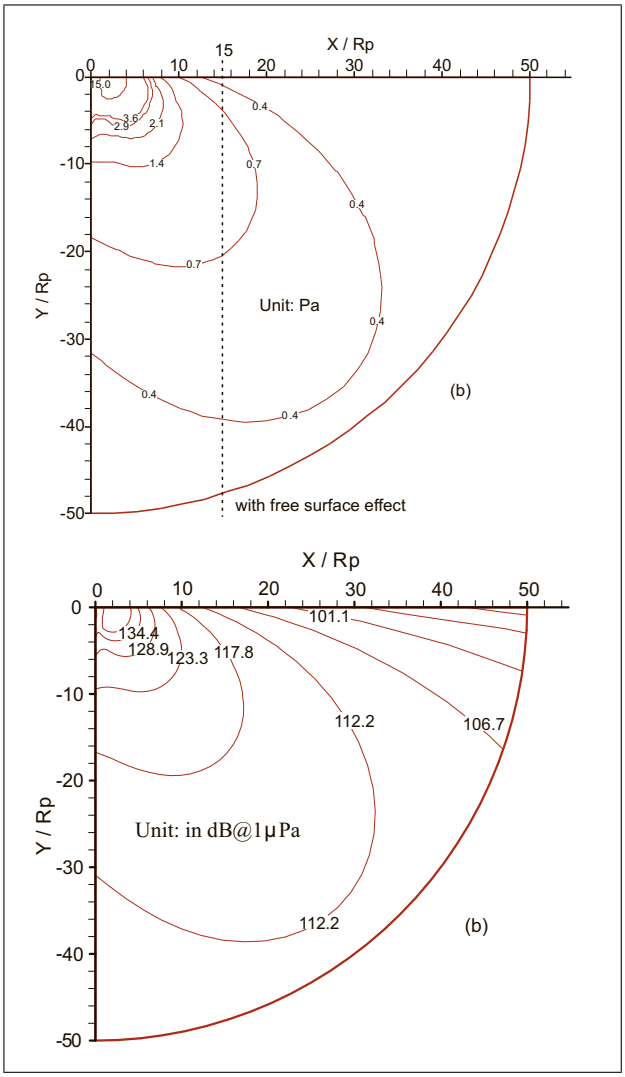


Figure 10. A contour plot of amplitude for the first blade-rate harmonic due to the propeller's unsteady thrust and torque force in the X-Y plane (unit: Pa).

right hand side of the Y-Z plane, (i.e. $\theta = 120$ degrees for the actual propeller). However, in Figure 9b they appear on the left-hand side of the Y-Z plane (i.e. $\theta_I = 303.6$ degrees for the imaged propeller), which can be explained on the basis of opposing angular directions of θ and θ_I as shown in Figures 9a,b. Additional details and the basis for this opposing angular direction are available in the published work of Kehr and Kao [7]. The total amplitude, shown in Figure 9c, is nearly symmetrical with respect to the Y-axis in the Y-Z plane.

The radiated noises caused by the propeller's unsteady thrust and torque force with the soft free surface are combined in Figures 10 and 11. The amplitude along the X-axis in Figure 10 is similar to that in Figure 6b, because the amplitude along the X-axis caused by the propeller's unsteady torque force in Figure 8b is relatively small. It is also found that the amplitude along the Y-axis in Figure 10 increases when the acoustic pressure due to the propeller's unsteady thrust and the torque force are both considered. The distribution of amplitude in Figure 11 forms concentric circles and is similar to those shown in Figures 7b and 9c.

6. Results of the scattered underwater acoustic field

Figure 12 shows the panelized geometry of this ship's hull with 960 hyperboloid panels. The convergence history for computation is shown in Figure 13. A grid dependence study is also conducted. Figure 13 indicates the convergent histories of scattered acoustic pressure from the ship's hull. As the coarse grids, 710 panels, are applied, the computing process shown in Figure 13 is divergent. It is found that the convergence is robust as the number of the cells is more than 960 panels. This robust convergence also results in consistent predictions as shown in Table I. In the present case, the total time steps over the maximum time period (0.578 sec) are 60 (i.e. in each iteration, 60 time steps are calculated) and only 9 times of iteration are required to achieve a convergent result. As the iteration times

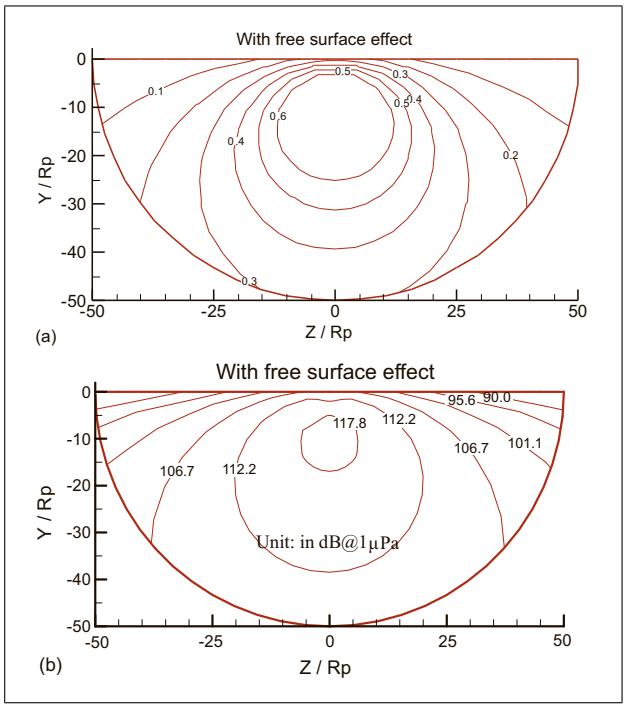


Figure 11. A contour plot of amplitude for the first blade-rate harmonic due to the propeller's unsteady thrust and torque force in the Y-Z plane at 15 Rp downstream from the propeller's center (unit: Pa).

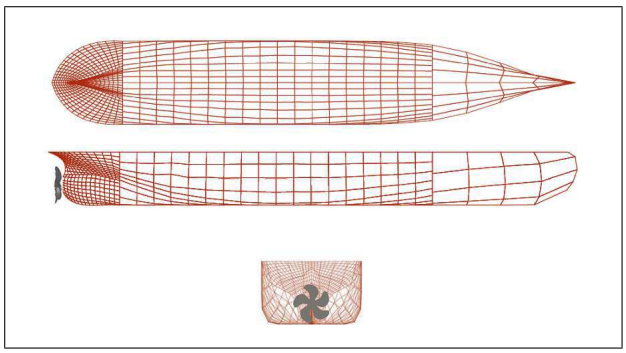


Figure 12. Discretized geometry of the ship's hull with 960 quadrilateral panels.

Table I. The convergence results for different panels. N: Number of panels. τ: Time steps in each iteration. M: Iteration times. P: Max. scattered pressure on the ship's hull (kPa) with soft free surface.

N	τ	M	P
960	60	20	0.689 (due to unsteady thrust) 0.218 (due to unsteady torque force)
1150	60	20	0.685 (due to unsteady thrust) 0.215 (due to unsteady torque force)

reach 9, the maximum difference in acoustic pressure on any panel between the n-th and $(n-1)$-th iterations is less than 10^{-4} Pa.

Figures 14 and 15 present the contour plots of the first blade-rate amplitude in the X-Y plane and in the Y-Z

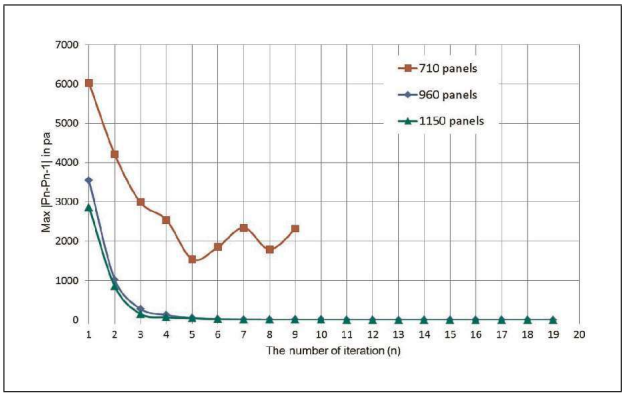


Figure 13. A contour plot of the first blade-rate pressure fluctuation on the stern due to the propeller's unsteady torque force (Unit: kPa; sound speed = 1500 m/s).

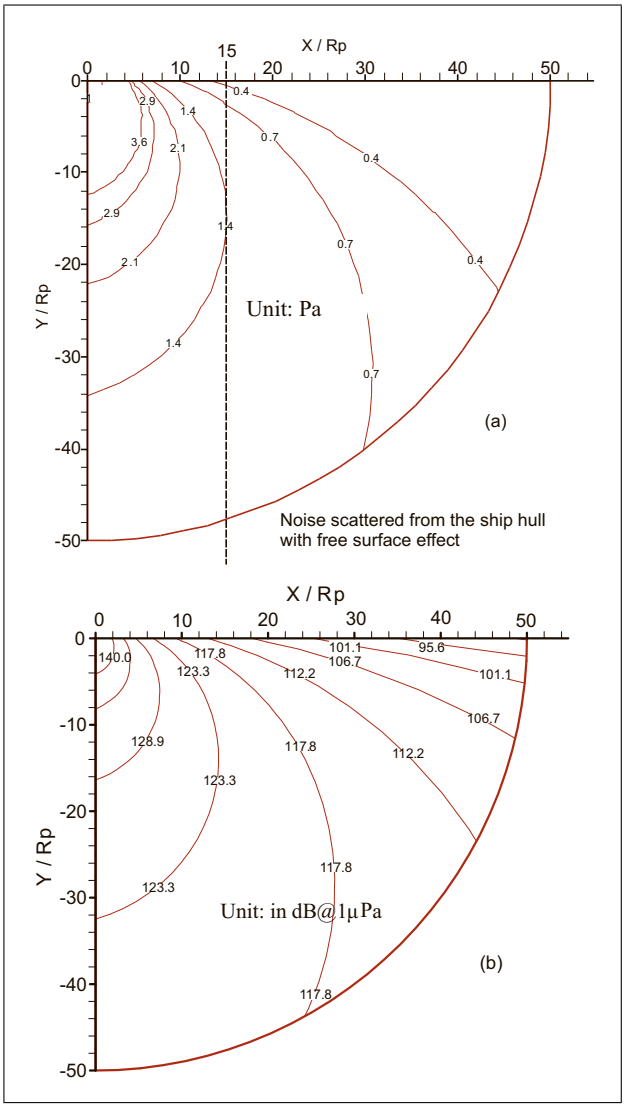


Figure 14. A contour plot of amplitude for the first blade-rate harmonic due to the pressure scattered from the ship's hull with a free surface effect in the X-Y plane (unit: Pa).

plane. The amplitude shown in Figures 14 and 15 is caused by the pressure scattered from the real and imaged ship

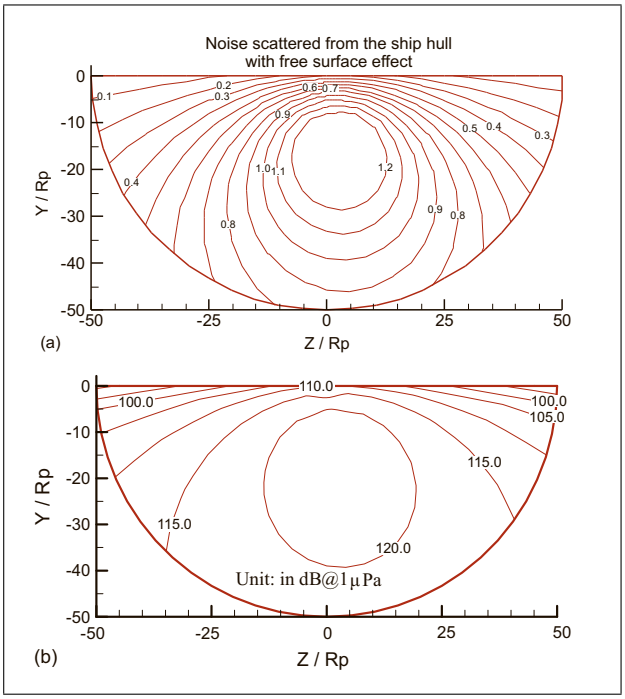


Figure 15. A contour plot of amplitude for the first blade-rate harmonic due to the pressure scattered from the ship's hull with a free surface effect in the Y-Z plane at 15 Rp downstream from the propeller's center (unit: Pa).

hulls; noise radiated from the real and imaged propellers is not included. The ship's hull is closer to the free surface than the propeller; therefore, the destructive interference along the propeller's axis due to the free surface, shown in Figure 14, is more serious than that shown in Figure 10. The dominant direction of the acoustic field caused by the pressure scattered from the ship's hull with a soft free surface is along the Y-axis in the X-Y plane. However, the amplitude along the Y-axis in Figure 14 is greater than the corresponding value in Figure 10 due to the opposite normal direction of the imaged ship's stern.

In the study by Kao and Kehr [8], if the scatterer is opposite the normal direction and accompanied by a soft free surface, then it will enhance the acoustic field. Please refer to the formulae in that study. The enhancement caused by the opposite from normal direction of the imaged ship's stern is very obvious. For example, at X=15 Rp, the amplitudes shown in Figure 14 are nearly two times those in Figure 10. Therefore, it is reasonable to assume that the amplitudes in Figure 15 (X=15 Rp) are nearly two times those in Figure 11 (X=15 Rp). Moreover, the contour lines in Figure 15 are almost symmetrical with respect to the Y-axis in the Y-Z plane due to the symmetry of the ship's hull and are similar to those shown in Figure 11.

Figures 16 and 17 illustrate the contour plots of the total first blade-rate amplitude, including the pressure field radiating directly from the propeller and scattered from the ship's hull with a soft free surface, at the same X-Y plane and Y-Z plane, as shown in Figures 10 and 11. By comparing Figures 16 and 10, it is noted that the amplitude in the X-Y plane is remarkably enhanced along the Y-axis. The

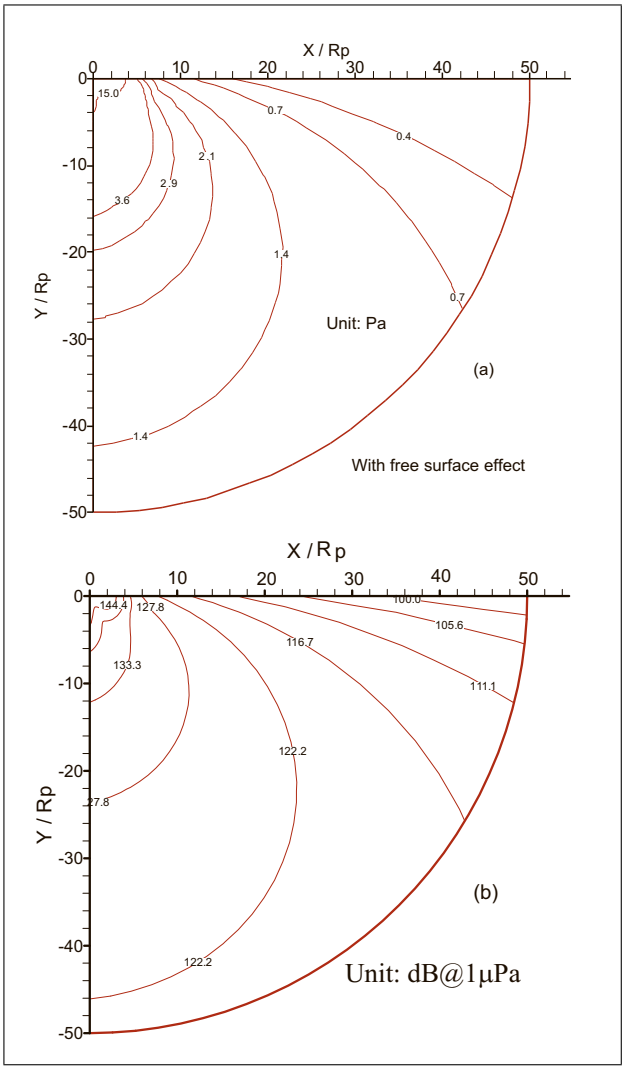


Figure 16. A contour plot of the amplitude for the first blade-rate harmonic due to the pressure radiated from the propeller and scattered from the ship's hull with a free surface effect in the X-Y plane (unit: Pa).

dominant direction of the acoustic field remains along the Y-axis in the X-Y plane, as shown in Figure 16.

The amplitude contour, shown in Figure 17, is obviously stronger, compared with Figure 11, due to the opposite to normal direction of the imaged ship's stern. Moreover, the contour lines in Figure 17 are symmetrical with respect to the Y-axis in the Y-Z plane, similar to those in Figure 11.

Kehr *et al.* [23] derived the higher-order panel method that satisfies the Laplace equation. Contour plots of the first blade-rate amplitude scattered from the ship hull in the X-Y plane and in the Y-Z plane are computed by the higher-order panel method, and the compared results are shown in Figures 18 and 19.

It is found that the contours near the propeller center are similar. As the field points are far enough, the difference between the results of the present method and the higher-order panel method are more and more remarkable due to the increment of the retard time, r/c. In [23], retard time, r/c, for wave propagation is not considered because

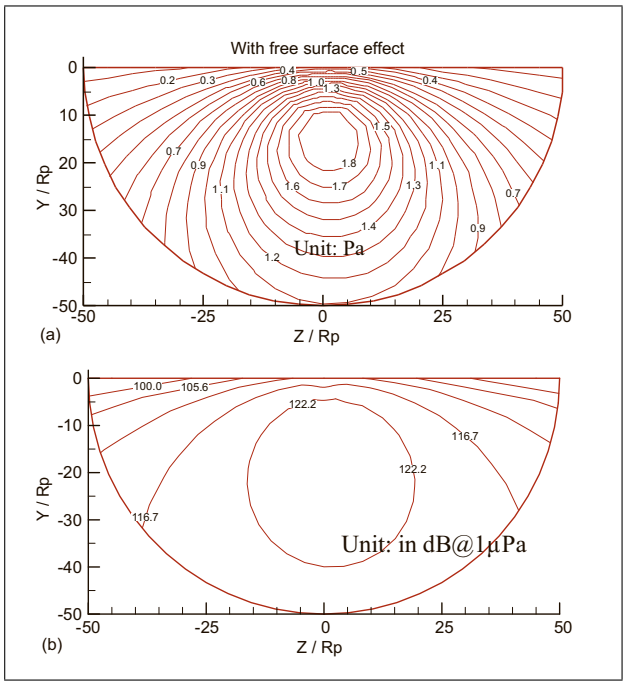


Figure 17. A contour plot of amplitude for the first blade-rate harmonic due to the pressure radiated from the propeller and scattered from the ship's hull with a free surface effect in the Y-Z plane at 15 Rp downstream from the propeller's center (unit: Pa).

incompressible flow is assumed. The same result can be obtained in Figure 19. It is evident that the scattered wave both for near and far fields can be predicted by the present scheme because the retarded time is considered accurately. However, the higher-order panel method can only be applied in the near field.

7. Conclusions

This paper solves the dipole noises that radiate directly from the propeller and are scattered from the ship's hull, both having a soft free surface. The scattering propagation of dipoles could be applied to remote sensing, sonar detecting, and marine environmental protection. Based on the above information, several points can be concluded as follows.

1. The acoustic pressure due to the propeller's unsteady thrust mainly depends on the axial direction of the field point and is dominant in the X-axis direction in the X-Y plane without a free surface effect. However, it is dominant in a direction that is about 45 degrees with the X-axis in the X-Y plane when a soft free surface is considered. The depth of the propeller center is 6.6 m. The interference of the real and the imaged propellers is dependent on the depth and the frequency. For other cases, the noise may not also dominate in the 45-deg direction.
2. The acoustic pressure, due to the propeller's unsteady torque force, depends on both the radial and angular positions of the field points. The interference caused by the free surface is strongly dependent on the angular position of the field point, θ. The constructive interference exists for field points, $\theta \approx 180$ degrees, when a soft free surface is considered. The acoustic pressure due to the propeller's unsteady torque force is dominant along the Y-axis in the X-Y plane.
3. The acoustic fields caused by the propeller's unsteady thrust and torque force are almost symmetrical with respect to the Y-axis in the Y-Z plane under the consideration of a soft free surface, and the interference is more obvious when the field points are close to the free surface.
4. The scattered wave is more sensitive to the free surface than the radiated wave, because the ship's hull is closer to the free surface. When the soft free surface is included, the scattering field is dominant in the Y-axis direction in the X-Y plan and symmetrical with respect to the Y-axis in the Y-Z plane.
5. The scattering field is strongly enhanced by almost two times when the soft free surface is considered. This en-

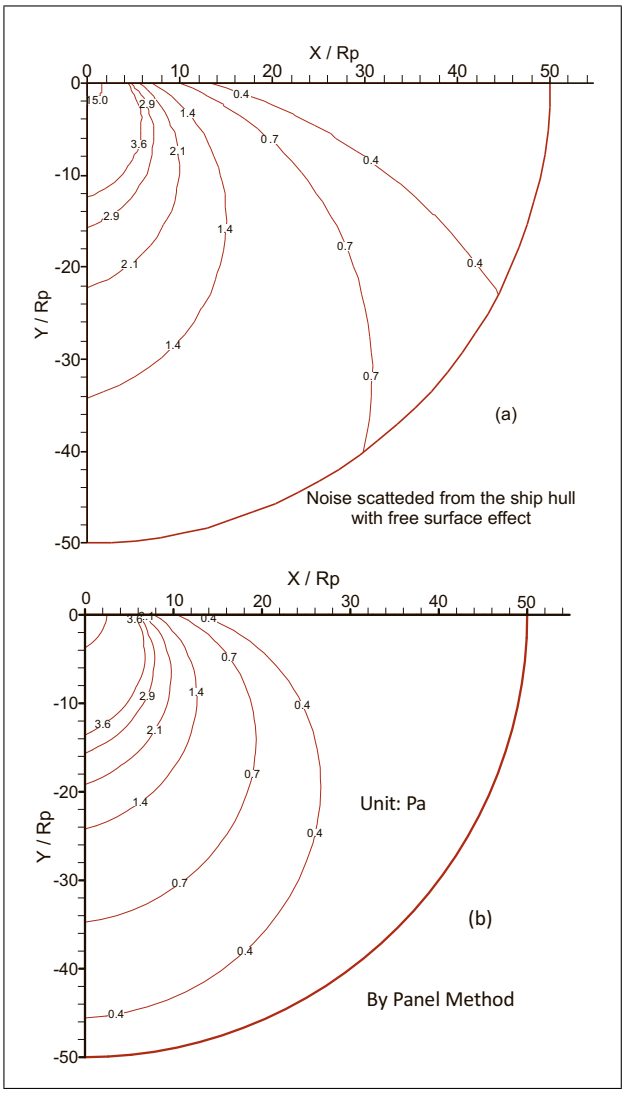


Figure 18. Comparision between the amplitudes for the first blade-rate harmonic due to the pressure scattered from the ship's hull with a free surface effect in the X-Y plane by different numerical methods.

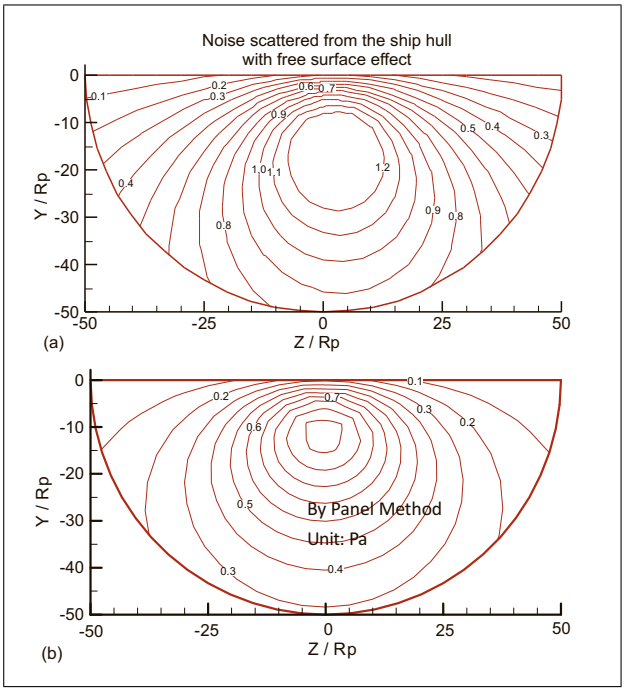


Figure 19. Comparision between the amplitudes for the first blade-rate harmonic due to the pressure scattered from the ship's hull with a free surface effect in the Y-Z plane at 15 Rp downstream from the propeller's center by different numerical methods.

hancement is caused by the opposite to normal direction of the imaged ship's stern, which is used to simulate the free surface.

6. When the radiated wave is added by the scattered wave with a free surface effect, the amplitudes in the acoustic field are remarkably increased. The amplitudes are then dominant along the Y-axis in the X-Y plane and are symmetrical with respect to the Y-axis in the Y-Z plane.

Acknowledgement

The author would like to express his thanks to the Ministry of Science and Technology, Taiwan for their financial support under contract number: MST-105-2221-E-019 -046.

References

[1] A. F. Seybert, B. Soenarko, F. J. Rizzo, D. J. Shippy: An advanced computational method for radiation and scattering of acoustic waves in three dimensions. The Journal of the Acoustical Society of America **77** (1985) 362–368.

[2] A. F. Seybert, B. Soenarko: Radiation and scattering of acoustic waves from bodies of arbitrary shape in a three-dimensional half space. ASME Trans. **110** (1988) 112–117.

[3] J. T. Chen, H. K. Hong: Boundary element method. Second edition. New World Press, Taipei, Taiwan, 1992.

[4] R. Kinns, C. D. Bloor: Hull vibration excitation due to monopole and dipole propeller sources. Journal of Sound and Vibration **270** (2004) 951–980.

[5] R. Spivack, O. R. abd Kinns, N. Peake: Acoustic excitation of hull surfaces by propeller sources. Journal of Marine Science and Technology **9** (2004) 109–116.

[6] O. R. Spivack, R. Kinns, N. Peake: Hull excitation by fluctuating and rotating acoustic sources at the propellers. 25th Symposium on Naval Hydrodynamics, 2004, 93–106.

[7] Y. Z. Kehr, J. H. Kao: Numerical prediction of the blade rate noise induced by marine propellers. Journal of ship research **48** (2004) 1–14.

[8] J. H. Kao, Y. Z. Kehr: A time-domain iteration method for acoustic scattering problems. Journal of ship research **50** (2006) 334–343.

[9] Y. Z. Kehr, J. H. Kao: Underwater acoustic field and pressure fluctuation on ship hull due to unsteady propeller sheet cavitation. Journal of Marine Science and Technology **16** (2011) 241–253.

[10] H. C. J. van Wijngaarden, Wageningen: Prediction of propeller-induced hull-pressure fluctuations. PhD thesis, TUD-Netherlands, 2011.

[11] D. R. Wilkes, A. J. Duncan: Application of the fast multipole boundary element method to underwater acoustic scattering. Australian Journal of Mechanical Engineering **8** (2011).

[12] C. X. Bi, L. Geng, X. Z. Zhang: Cubic spline interpolation-based time-domain equivalent source method for modeling transient acoustic radiation. Journal of Sound and Vibration **332** (2013) 5939–5952.

[13] K. Paula, T. Osman, I. Atilla: A study of numerical ship underwater noise prediction. Ocean Engineering **66** (2013) 113–120.

[14] J. S. Jang, H. T. Kim, W. H. Joo: Study on non-cavitating noise of marine propeller. 43rd International Congress on Noise Control Engineering Improving the World through Noise Control, Melbourne, Australia, 16–19 November 2014.

[15] S. Ianniello: The underwater noise prediction from marine propellers: an essentially nonlinear problem. The 21st International Congress on Sound and Vibration, Beijing/China, 13-17 July 2014.

[16] J. Li, D. Dault, B. Shanker: A quasianalytical time domain solution for scattering from a homogeneous sphere. The Journal of the Acoustical Society of America **135** (2014) 1676–1685.

[17] J. H. Kao: A weighting-iteration method in the time domain for solving the scattering problem of a complex-shaped. Engineering Analysis with Boundary Elements **62** (2016) 7–12.

[18] J. E. Kerwin, C. S. Lee: Prediction of steady and unsteady marine propeller performance by numerical lifting surface theory. Society of Naval Architects and Marine Engineers Transactions **86** (1978) 218–253.

[19] P. M. Morse, K. U. Ingard: Theoretical acoustics. Princeton University Press, Princeton, N.J., 1968.

[20] W. K. Blake: Aero-hydroacoustics for ships. david taylor naval ship research and. Development Center, Washington, D.C. Vol. 2, 1984.

[21] M. Stütz, M. Ochmann, M. Möser: Improving stability of the transient boundary element methodusing the CHIEF-method. Congress in Sound and Vibration, Ljubljana, Slovenia, 15-18 Sep. 2010.

[22] D. J. Chappell, P. J. Harris, D. R. Henwood, Chakrabarti.: A stable boundary element method for modeling transient acoustic radiation. JASA **120** (2006) 74–80.

[23] Y. Z. Kehr, C.-Y. Hsin, Y.-C. Sun: Calculations of pressure fluctuations on the ship hull induced by intermittently cavitating propellers. Proc. Natl. Sci. Counc. ROC (A) **22** (1998) 642–653.